Data Processing Techniques for Airport Surveillance Radar Weather Sensing *

Mark E. Weber, Richard L. Delanoy, Edward S. Chornoboy
Lincoln Laboratory
Massachusetts Institute of Technology
Lexington, Massachusetts

1. Introduction

In his review paper on applications of meteorological Doppler radar for weather surveillance near air terminals, Strauch [1] identified a number of areas where such radars could provide important operational benefits. Subsequent implementation of the Federal Aviation Administration's (FAA) Terminal Doppler Weather Radar (TDWR) will bring capabilities such as automated storm identification and tracking and detection of low altitude wind shear to large airport terminals. Cost considerations, however, have prevented implementation of these advanced weather detection capabilities across the U.S. airspace system.

In this paper we discuss data processing techniques that can provide high quality, automated weather information using the FAA's existing Airport Surveillance Radars (ASR-9). The cost of modifying the ASR-9 is significantly less than that for deployment of the dedicated TDWR. These techniques have been implemented on a prototype ASR-9 Weather Surveillance Processor (WSP) and have been tested operationally for each of the last five summers at the Orlando, FL and Albuquerque, NM Air Traffic Control towers. Key to the success of this system has been the development of innovative data processing techniques that accommodate the non-optimum parameters of the ASR as a weather sensor.

Data processing challenges fall into two areas. Time-series signal processing of the received weather echo samples are required to accomplish ground clutter suppression and estimation of weather reflectivity and radial velocity. The ASR-9's rapid scan rate and variable pulse repetition frequency (PRF) waveform preclude the use of conventional ground clutter filter designs and "pulse-pair" or fast Fourier Transform (FFT) based weather spectrum moment estimation. Accurate measurements of "microburst" outflow winds–a phenomenon confined to the lowest 100-500 m of the atmosphere–is complicated by the contamination of the outflow Doppler signal by echoes from precipitation aloft entering the broad surveillance beam at a higher elevation angle. These interfering signals are normally at a markedly different Doppler velocity than the outflow and will prevent accurate measurement of the near-surface radial wind velocity if conventional mean-velocity estimators are employed. "Gust fronts" and "dry" microbursts (divergent outflows associated with little or no rain at the surface) produce signals that are often near the system noise level and may be fragmented by ground clutter, second-trip weather echoes and other forms of interference. Accurate estimation of signal parameters at very low signal-to-noise ratio (SNR)–given limited data samples–poses a significant challenge.

Image processing algorithms automatically extract operationally relevant information from the reflectivity and radial velocity images and allow for its rapid dissemination to Air Traffic Controllers and other users. Owing to the above-described signal processing issues, these input images may be corrupted by noise, ground clutter residue or weather echoes from aloft that do not reflect the relevant near-surface wind field. "Machine intelligent" image and expert system processing has been employed extensively in the WSP system to allow for detection of subtle microburst and gust front signatures. This technology, derived from work at our Laboratory in Automatic Target Recognition [2], has proven capable of equaling or exceeding the performance of humans in recognizing relevant features in the data field.

In this paper, we motivate the development of the ASR-9 WSP system and describe in detail the data processing techniques that have been employed to achieve an operationally useful capability. Section 2 provides an overview of the WSP and our ongoing system development and test program. In section 3 we provide specifics on the data processing algorithms that have been key to successful implementation of this capability.

2. Airport Surveillance Radar Weather Surveillance Processor

A *microburst* occurs when an intense, small-scale downdraft from a thunderstorm reaches the earth's surface and diverges horizontally in a cylindrically symmetric pattern. Penetrating aircraft encounter a rapid headwind to tailwind transition and associated downdraft; an aircraft at low altitude on final approach or takeoff may not be able to recover from the resulting loss of altitude and climb capability. *Gust fronts* are thunderstorm outflows whose leading edges propagate away from the generating precipitation, creating a convergent wind shear along the leading edge and a subsequent shift in wind speed and direction. Tracking and predicting gust front arrivals before the front reaches an airport allows for more efficient use of runways.

The WSP modification to the ASR-9 will provide the functional capabilities of the TDWR at airports whose operation levels and/or thunderstorm exposures do not justify the costs of the dedicated radar. The system provides automatic detection and warning of microburst wind shear, tracking of gust front wind shifts and predictions of their impact at the airport, and predictions of the movement of

* This work was sponsored by the Federal Aviation Administration. The views expressed are those of the authors and do not reflect the official policy or position of the U.S. Government.

0-7803-2120-0/95/0000-0521 $4.00 © (1995 IEEE)

thunderstorm cells. The modification will also allow for suppression of ground clutter breakthrough during anomalous propagation conditions.

An experimental Airport Surveillance Radar facility has supported weather data collection for use in development and validation of the WSP's signal processing and meteorological detection algorithms, and operational demonstration of WSP products at actual Air Traffic Control towers. This facility has been operated since 1987 at four different sites to characterize performance in diverse environments. Pencil-beam Doppler weather radars and an anemometer network have been operated at each site to provide the meteorological "truth" necessary for development and validation of the WSP algorithms. In addition, the WSP has been evaluated operationally each year since 1990 through display and utilization of its products in the ATC facilities in Orlando and Albuquerque.

Overall, the technical performance of the system has been excellent, approaching that of the TDWR in southeastern U.S. environments where wind shear is typically associated with moderate to high radar reflectivity. Operational acceptance of the system by Air Traffic Controllers at both Orlando and Albuquerque has been excellent; significant benefits accrue from not only the safety-related information provided by the WSP (e.g., microburst warnings) but also from enhanced weather situational awareness provided by its broad-area graphical display of significant weather events in terminal airspace. A more extensive discussion of our development and test activities is provided in [3].

3. Data Processing Techniques

(a) Variable PRF Coherent Processing

The ASR-9 radar has a high scan rate (12.5 RPM) and utilizes a block-staggered sampling strategy to mitigate aircraft blind speeds. The confines of a single uniform-spaced block (eight or ten pulses) do not provide a coherent gain sufficient for meteorological detection and estimation. To adapt to the ASR-9, it has been necessary to develop processing strategies that treat its returns coherently across changing PRF boundaries.

The single-lag autocorrelation method known as pulse pair is the most widely used method for estimating meteorological spectral moments. Given pulse spacing T_1, and autocorrelation-lag estimate $\hat{R}_1 = \hat{R}(T_1)$, the first moment, or Doppler velocity, is given by $\hat{V}_1 = -(\lambda / 4\pi T_1) \arg(\hat{R}_1)$, where λ is the radar wavelength. When lag estimates from two relatively prime spacings are available ($T_1 > T_2$ and $T_1/T_2 \neq m$ for any integer m), it is common for meteorological processors to extend the interval of unambiguous Doppler through consideration of the folding residues observed with independent estimates $\hat{V}_1$ and $\hat{V}_2$. This fundamental concept is illustrated in Figure 1a for reference.

Dedicated meteorological radars typically rely on high-pass prefilters for suppression of stationary ground clutter; a filter extending across the ASR-9's block-staggered boundaries must have (periodically) time-varying coefficients. Filters that achieve but a desired magnitude response introduce estimation errors owing to the phase distortion that accompanies nonuniform pulse spacing. Without linear phase, the above-described conventional dealiasing fails as well.

To control estimation error and reconcile velocity dealiasing with time-varying clutter filters it is necessary to do complex-domain filter design. Depending on the dealiasing method, additional control of the filter phase response, relative to magnitude error, is also required [4, 5, 6]. Design of the phase response must be balanced against the introduction of "blind speeds" in the magnitude response. When error types are appropriately distributed across the filter's coefficient sets, one can obtain average response profiles that restore the dealiasing capability of multi-PRF–with good approximation to a uniform passband over a greatly extended bandwidth (compare Figures 1a and 1b).

The low signal strengths associated with gust fronts and dry microbursts has motivated additional experimentations with "fully coherent" processing–the estimation of Doppler spectra from an ASR-9's nonuniformly spaced pulse samples. As described in [7] Doppler velocity estimates derived from frequency domain signal representations may achieve lower estimate standard errors–at a given SNR–than the pulse pair algorithm. With variable pulse spacings, band-limited extrapolation [8] can be used to define appropriate "DFT" transforms [9, 10]. These, in turn, offer a new method for extending the unambiguous Doppler interval of the radar.

The method is illustrated in Figure 2. Because the ASR-9's two PRFs have the relationship 7:9 (with the longer pulse spacing approximately 1 msec), the collected data can be superimposed on a much finer uniform sampling grid with pulse spacing 1/9 msec. These "complete" data would have 215 pulse samples and yield a Nyquist interval on the order of ±234 m/s. With an appeal to a minimum-norm pseudo-inverse, one can estimate a spectrum even if the total number of time samples is but 27, as is the case with the ASR-9. Such an estimate is shown in the upper left panel (only the range ± 100 m/s is shown). With uniform sampling, such an estimate would exhibit exact replication in regions of aliased energy. The nonuniform spacing causes aliased energy to appear whitened. In this simulated example, the true centering Doppler is 65 m/s (vertical line and "+" symbol in figure) with a spectrum width of 6 m/s (the SNR is 5 dB).

Noting that actual meteorological echoes will be confined to a spectral interval much smaller than the +/-100 m/s domain shown, we can use the technique of band-limited extrapolation to recompute spectra confined to smaller Doppler intervals around candidate peaks.

Examples are shown in the remaining panels; the inset numbers are respectively the mean and widths of the recomputed spectra. Discrimination of the true Doppler spectrum from aliases is accomplished on the basis of their computed spectrum spread. The true Doppler centering frequency is inferred by selection of that spectrum with least spread. Figure 3 illustrates the expected performance from Monte Carlo simulation work. The figure shows excellent performance over a wide range of meteorological spectrum widths and down to SNR values as low as 5 dB. Further improvement in dealiasing accuracy at low SNR can be realized through application of the concepts of [7] in computing the spectrum width.

(b) Mixture Density Wind Component Extraction

Observations with pencil-beam Doppler weather radars have shown that the divergent outflow in microbursts is confined to a shallow altitude interval extending upwards from the surface. Range height indicator (RHI) scans of microbursts occurring within 10 km of a 1 degree pencil-beam Doppler weather radar (i.e., vertical resolution of 200 m or less) were analyzed in [11]. The median height of the maximum outflow differential velocity was about 50 m, and the median height at which the outflow strength dropped to one-half of its maximum value was about 500 m. Figure 4 (from [12]) plots vertical distributions of radial velocity through three example microbursts.

In this scenario where the radial wind component varies rapidly with altitude an ASR's cosecant squared elevation beam pattern (5 degree half-power width) intercepts scatterers moving at both the near-surface radial velocity and at the velocity of the wind aloft. The result is a broad, possible multi-modal velocity spectrum whose power-weighted mean–the conventional weather radar Doppler velocity estimator [13]–can differ markedly from the near-surface radial wind velocity. Figure 5 shows examples of such spectra measured with both the "high" and "low" beams of our experimental ASR. The spectra were estimated from Discrete Fourier Transforms of 34-sample Hamming windowed data sequences, incoherently averaged over three contiguous range gates. Ground clutter, where present, has been adaptively filtered from the spectra [14]. For reference, the dashed vertical lines indicate the true near-surface radial velocity, measured with a pencil-beam radar co-located with the ASR.

Extraction of the appropriate low-altitude components of these "mixture density" spectra is accomplished through comparison of signals received near-simultaneously in the high and low elevation beams of the ASR. As shown in Figure 6, the gain of these two patterns differs significantly below 5 degrees; this design allows the aircraft detection channel to reduce ground clutter illumination by receiving on the high beam at short range. Our WSP modification includes switches and couplers so that both high- and low-beam data are available for processing.

Comparison of the spectra plotted in Figure 5 with the gain patterns of Figure 6 indicates that discrimination between near-surface echoes and those from higher altitude can be accomplished using the relative amplitudes of high- and low-beam power spectrum densities (PSD). However, low-altitude velocity estimators based on the PSDs are somewhat unstable statistically (a problem that is exacerbated by the short coherent processing intervals available from the ASR), and are computationally expensive. We have implemented an efficient algorithm for low-altitude velocity estimation based on parametric modeling of the low- and high-beam spectra [15]. Consistent with many of the measured spectra, we model the PSD of weather signals received by the ASR as the summation of two Gaussian components:

$$S_i(f) = \frac{a_{i,1}}{\sqrt{2\pi}\sigma_1} \exp\left[\frac{-(f-f_1)^2}{2\sigma_1^2}\right] + \frac{a_{i,2}}{\sqrt{2\pi}\sigma_2} \exp\left[\frac{-(f-f_2)^2}{2\sigma_2^2}\right] \quad (1)$$

where i=1, 2 indexes the low and high receiving beams. The center frequencies f_i and widths of σ_i the two spectral components are assumed to be identical between the two beams but the amplitudes ($a_{i,1}$ and $a_{i,2}$) will differ owing to the different weightings from the antenna patterns.

In [15], we describe methods of estimating the eight parameters in equation (1) using measurements of the low- and high-beam autocorrelation functions at lags of zero through two times the average pulse repetition interval. The solutions are constructed using knowledge of the beam patterns so that the parameters $a_i,1$, σ_1 and f_1 represent the spectral component associated with scatterers at low elevation angle. Figure 7 plots the resulting parametrically modeled power spectra for the microburst cases shown in Figure 5. Although these are not optimum fits (for example in a least squares sense) they generally correspond well to the data. The desired low altitude velocity estimate– f_1–is obtained directly as one of the parameters of the model.

Results from Monte Carlo simulations of this estimator's bias and standard deviation for a representative microburst velocity profile are shown in Figure 8. Consistent with analysis of field data collected over eight years with our experimental ASR, the plot indicates good performance: biases relative to true near-surface outflow velocity are 5 m/s or less and standard deviations of the estimates are 3 m/s or less. As discussed in [3], this level of accuracy for the surface velocity estimator has supported microburst detection probabilities for the ASR-9 WSP that are well above 0.9 under high SNR conditions.

(c) Machine Intelligent Gust Front Detection

Gust front detection and tracking for the WSP is accomplished through computer recognition of the line of enhanced signal strength–the "thin line echo"–that forms at the leading edge of gust fronts owing to concentration of particulate scatterers (e.g., insects) by the convergent winds. This subtle feature produces a slight enhancement of radar reflectivity and/or a line of spatially coherent velocities embedded in a background where the gate-to-gate estimate variance is much higher. Movement of thin lines through a

background of stationary ground clutter or more slowly moving storm cells aids in their identification.

Automated gust front detection algorithms developed previously for the National Weather Service's NEXRAD and the TDWR [16, 17] were not successful when applied to reflectivity and Doppler velocity imagery generated from the ASR-9. These algorithms have relied heavily on direct measurement of the convergent wind pattern associated with a gust front, a feature that is often not measurable with an ASR owing to low SNR. Their thin line detection processing likewise performed poorly owing to its not making use of all the gust front features available in the ASR imagery and to sequentially applied thresholds that discarded relevant information at early stages of the processing.

The machine intelligent gust front algorithm (MIGFA) developed subsequently for the WSP uses a bank of parallel "feature detectors" that are selectively indicative of the thin line object being sought. Knowledge of the characteristics of this object is incorporated in these detectors through the design of matched filters that are customized not only to this object but also to the physical properties of the sensor and the environment. A new technique of knowledge-based signal processing, called functional template correlation (FTC), allows for the construction of customized signal processing operations that are more effective than standard operations. The output of the FTC is a map of numeric values in the range [0, 1] that indicates the degree of match between the pattern of pixels in an image region and the feature or object encoded in the functional template. Figure 9 illustrates the functional template that is used for thin line detection in reflectivity imagery. Note that high "scores" are returned, for example, when the FTC kernel is centered on a linear feature with reflectivity values characteristic of gust front thin lines (5-15 dBz) and when surrounding values are near the background noise level (< 0 dBz).

Figure 10 is a system block diagram of MIGFA. In preparation for processing, input Doppler velocity (V) images and reflectivity (DZ) images are converted from polar to Cartesian representations. The velocity image is converted to a map of local standard deviation (SD). The SD and DZ images are then passed to multiple independent feature detectors, most of which are based on FTC. The different "interest" images so produced are fused to form a combined interest image indicating the location of possible gust fronts. From the combined interest image, fronts are extracted as chains of points. These chains are combined with those detected on prior scans by establishing a point-to-point correspondence, and thereby a "gust front history." The updated history is used to make predictions of where points along the front will be located at future times. This prediction serves both as an operational product to facilitate preparation for gust front arrivals at an airport and as an input to the "ANTICIPATION" interest image that heightens MIGFA's sensitivity where fronts are expected to be.

Figure 11 illustrates MIGFA's feature detectors for a case involving two gust fronts intersecting near the radar. Input DZ and SD images show weak evidence for the fronts, but occluding storm cells, ground clutter and second trip weather echoes introduce considerable ambiguity. The third through sixth panels in the figure show the outputs of the feature detectors searching, respectively, for reflectivity and velocity image thin lines and for their motion. In this example, the strongest evidence for the fronts comes from the ANTICIPATION image, where consistent previous history for the fronts has generated strong interest at their current locations. Negative interest from the out-of-trip weather detector suppresses potential false alarms caused by elongated echoes from these distant storms. The final combined interest image, when thresholded at the 0.5 level of ambiguity, yields a reasonably clear detection of both fronts. Subsequent feature extraction and chain extension processing fills in gaps in the detected fronts and extends them in length.

MIGFA significantly outperforms the earlier gust front algorithms. Table 1 compares its detection and false alarm performance against the most capable of the preceding algorithms–the so-called Advanced Gust Front Detection Algorithm or AGFA [17]. The test set consists of nine moderately strong gust fronts tracked through 15 hours (372 images input to the algorithms). A human interpreter generated "truth" by examining time-coincident imagery collected by a more sensitive pencil-beam Doppler weather radar. Relative to the baseline, MIGFA nearly doubled the overall event probability of detection while maintaining a very low false-alarm rate. It approximately tripled the percentage of gust front length detected for the test set.

Table 1.
AGFA and MIGFA Performance*
on ASR-9 WSP Data

	Gust Fronts		Gust Front Length	
	Probability of Detection (POD)	Probability of a False Alarm (PFA)**	Percent Length Detected (PLD)	Percent False Length Detected (PFD)
Baseline (AGFA)	42.6	3.2	21.0	4.2
MIGFA	75.1	0.0	58.7	6.4
* As scored against human interpretations of matching TDWR data				
** Expressed as a percent				

4. Summary

A dual use for the ASR-9 as a capable, Doppler weather radar providing operationally oriented meteorological information for air terminals has been achieved in the face of significant technical challenges. Analysis and on-line testing with our prototype ASR-9 WSP has confirmed that the system can provide reliable detection of low-altitude wind shear and enhanced overall weather situational awareness for Air Traffic Control teams. Innovative signal and image processing algorithms have been required to cope with the parameters of this aircraft search radar. Algorithm refinement is ongoing, with emphasis on improved detection and prediction of wind shear phenomena in challenging environments such as the U.S. Midwest and High Plains.

Several of the processing techniques developed for the WSP are applicable to other systems. Our techniques for

coherently processing across the variable PRF waveforms transmitted by ASRs are being investigated in the context of range/Doppler velocity ambiguity removal for weather radar [18]. Adaptations to the Machine Intelligent Gust Front Algorithm are proving very beneficial to TDWR and NEXRAD for wind shift prediction and for delineation of outflow boundaries that are the preferred locations for new convective development.

References:

[1] R.G. Strauch, "Applications of meteorological Doppler radars for weather surveillance near air terminals," *IEEE Transactions on GeoScience Electronics*, GE-17, 105,1979.

[2] J.G. Verly, R.L. Delanoy, D.E Dudgeon, "Machine intelligence technology for automatic target recognition," *Lincoln Laboratory Journal*, 2, 277, 1989.

[3] M.E. Weber, M.L. Stone, "Low altitude wind shear detection using airport surveillance radars," 1994 IEEE National Radar Conference, 29-31 March 1994, Atlanta, GA.

[4] E.S. Chornoboy, "Clutter filter design for multiple-PRT signals," Preprints: *26th International Conference on Radar Meteorology*, pp. 235-237, 1993.

[5] E.S. Chornoboy, "Optimum time-varying FIR filter designs for the airport surveillance radar wind shear processor," Lexington, MA, MIT Lincoln Laboratory, ATC Report 191, 1994.

[6] E.S. Chornoboy, "FIR design methods for non-uniformly sampled signals," Lexington, MA, MIT Lincoln Laboratory, Technical Report 976,

[7] E.S. Chornoboy, "Optimal Mean Velocity Estimation for Doppler Weather Radars," IEEE Transactions on Geoscience and Remote Sensing, vol. 31, no., 3, May 1993.

[8] A.K. Jain and S. Ranganath, "Extrapolation algorithms for discrete signals with application in spectral estimation," *IEEE Transactions on Acoustics, Speech, and Signal Processing*, vol. ASSP-29(4), pp. 830-845, 1981.

[9] M.E. Weber and E.S. Chornoboy, "Coherent processing across multi-PRI waveforms," Preprints: *26th International Conference on Radar Meteorology*, pp. 232-234, 1993.

[10] E.S. Chornoboy and M.E. Weber, "Variable-PRI processing for meteorologic Doppler radars," IEEE National Radar Conference, pp. 85-90, 1994.

[11] P.J. Biron, M.A. Isaminger, "High resolution microburst outflow vertical profile data from Huntsville, Alabama and Denver, Colorado," Lincoln Laboratory Project Report, ATC-163, FAA-PS-88-17, 1991.

[12] M.E. Weber, W.R. Moser, "A preliminary assessment of thunderstorm outflow wind measurement with airport surveillance radars," Lincoln Laboratory Project Report, ATC-140, FAA-PM-86-38, 1987.

[13] D.S. Zrnic, "Estimation of spectral moments for weather echoes," *IEEE Trans. on GeoSc. Electronics*, GE-17, 113, 1979.

[14] M.E. Weber, "Ground clutter processing for wind measurements with airport surveillance radars," Lincoln Laboratory Project Report ATC-143, FAA-PM-87-21, 1987.

[15] M.E. Weber, "Dual-beam autocorrelation based wind estimates from airport surveillance radar signals," Lincoln Laboratory Project Report ATC-167, FAA-PS-89-5, 1989.

[16] H. Uyeda and D.S. Zrnic, "Automated detection of gust fronts," *Journal of Atmospheric and Oceanic Technology*, 3, 36, 1986.

[17] M. Eilts, S. Olson, G. Stumpf, L. Hermes, A. Abrevaya, J. Culbert, K. Thomas, K. Hondl and D. Klingle-Wilson, "An improved gust front detection algorithm for the TDWR," *Proceedings of the Fourth International Conference on Aviation Weather Systems*, Paris, France, June 1991.

[18] E.S. Chornoboy, M.E. Weber, "Variable-PRI processing for meteorological Doppler radar," 1994 IEEE National Radar Conference, 29-31 March 1994, Atlanta, GA.

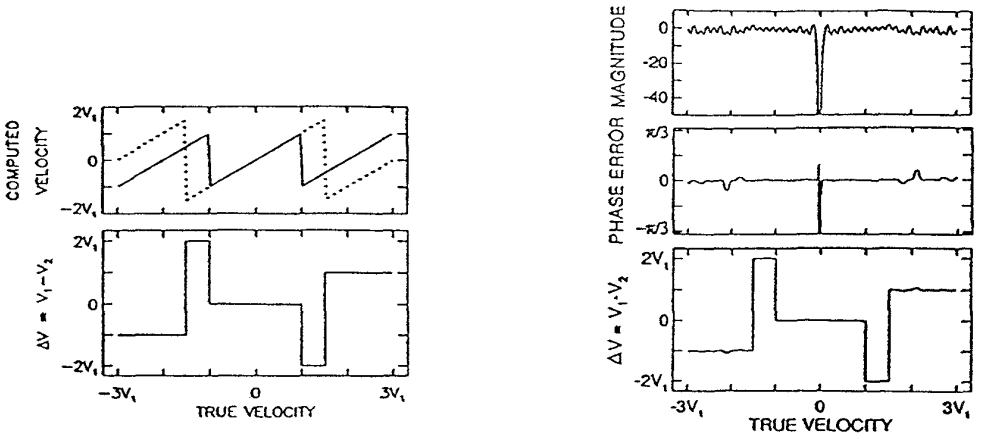

(a) (b)

Figure 1: (a) Ideal dealiasing using ΔV method. (b) Filter response and ΔV transfer function for block-staggered design with phase control.

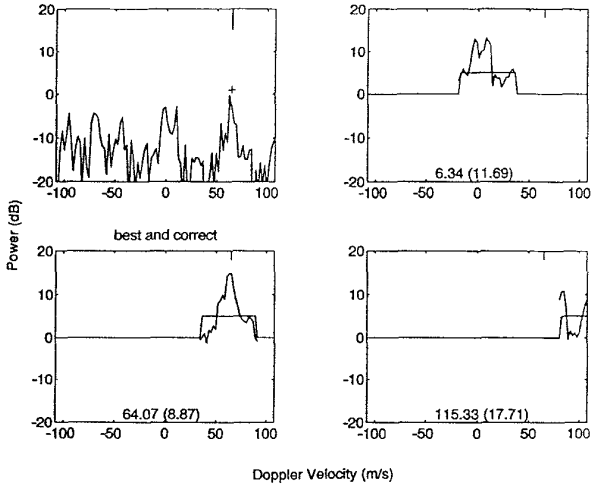

Figure 2. Variable-PRF discrete Fourier transform of a simulated weather signal plus noise as described in the text.

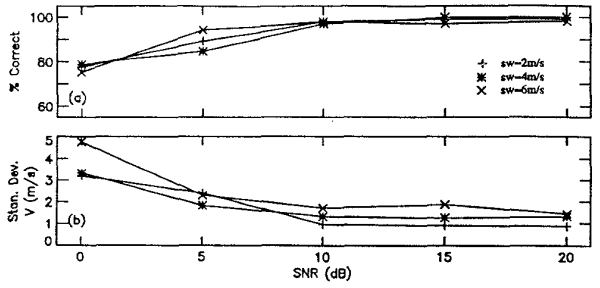

Figure 3. Probability of correct unfold and associated Doppler velocity estimate standard deviation using the fully coherent dealiasing method described in the text. Simulation weather signals are at a mean Doppler-velocity of 55 m/s.

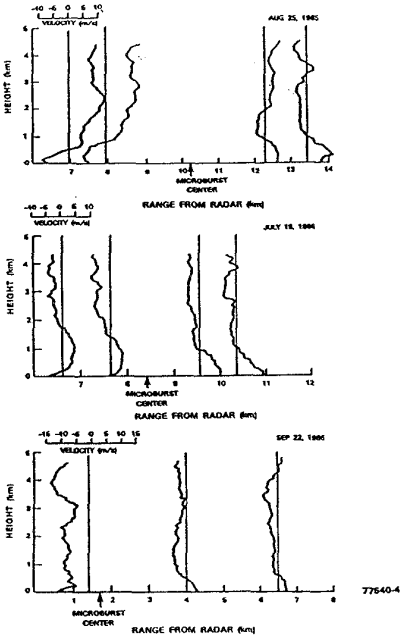

Figure 4. Vertical distribution of the radial wind speed of three microbursts, measured with a 1 degree pencil-beam Doppler weather radar. The horizontal distance from the radar to each profile is indicated by the associated vertical line. This line also marks the zero point for the radial velocity scale.

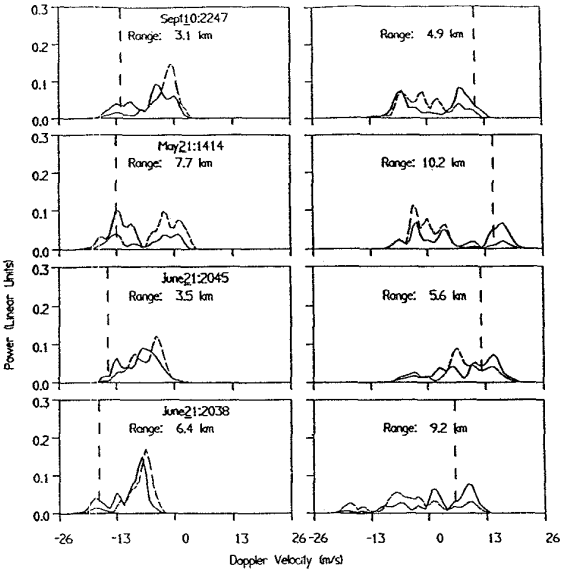

Figure 5. Variable-PRF discrete Fourier transform of a simulated weather-signal plus noise as described in the text.

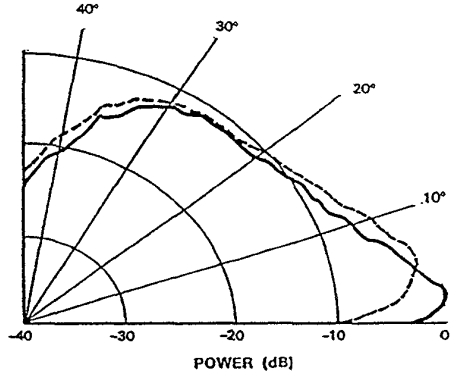

Figure 6. ASR-9 elevation beam patterns. Low and high beams plotted with solid and dashed lines, respectively.

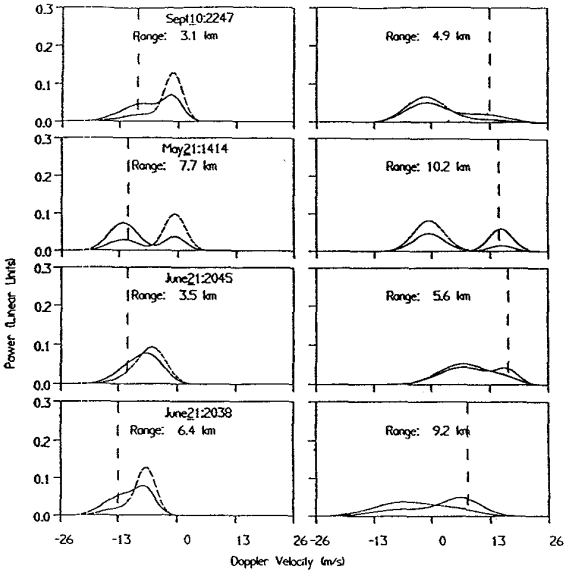

Figure 7. Velocity spectra reconstructed from ASR autocorrelation lag measurements as described in the text. The microburst examples and plot format are as in Figure 2.

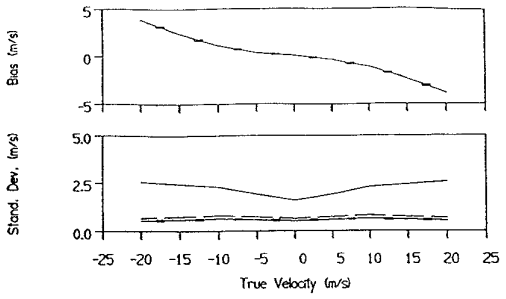

Figure 8. ASR low-altitude velocity estimate bias and standard deviation as a function of near-surface radial velocity. Plots were generated using a Monte Carlo simulation and a representative microburst radial velocity and reflectivity height distribution.

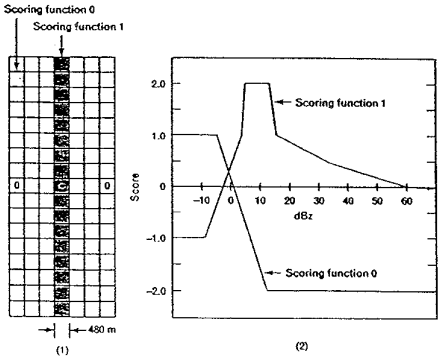

Figure 9. Example functional template for thin-line feature detection. Left panel shows the kernel which is passed over the image at varying orientations. Corresponding scoring functions for the "thin-line" (1) and "background" (0) pixels of the kernel are shown in the right panel.

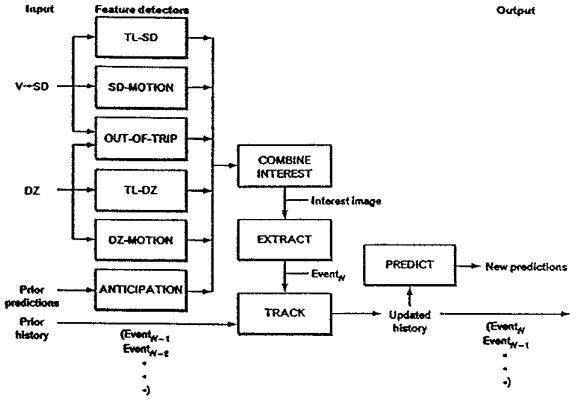

Figure 10. Block diagram of MIGFA.

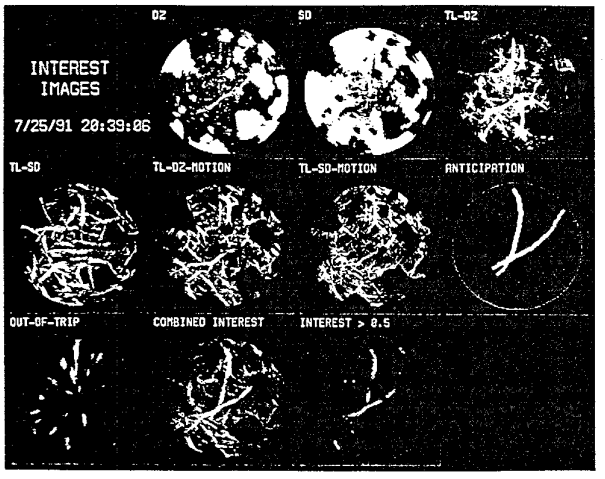

Figure 11. Example of input imagery and "interest images" generated by MIGFA feature detectors.